Tailoring α-MnO$_2$ gas diffusion electrodes for enhanced oxygen reduction in aluminum-air batteries

Alexander Rampf [a,b], Robert Leiter [a], Simon Fleischmann [a], Giuseppe Antonio Elia [c], Roswitha Zeis [a,b,d,*]

[a] Helmholtz Institute Ulm, Karlsruhe Institute of Technology, Helmholtzstraße 11, 89081 Ulm, Germany
[b] Department of Electrical Engineering, Friedrich-Alexander-Universität Erlangen-Nürnberg, Cauerstraße 9, 91058 Erlangen, Germany
[c] GAME Lab, Department of Applied Science and Technology (DISAT), Politecnico di Torino, Corso Duca degli Abruzzi 24, 10129 Torino, Italy
[d] Department of Mechanical and Industrial Engineering, University of Toronto, 5 King's College Road, Toronto, Ontario M5S 3G8, Canada

ABSTRACT

α-MnO$_2$ is a promising, inexpensive, and readily producible catalyst for the oxygen reduction reaction (ORR) in alkaline media, but its application is limited by low electronic conductivity. In this study, we enhance the performance of α-MnO$_2$ electrodes by systematically varying the α-MnO$_2$-to-Vulcan ratio within the catalyst layer. Electrodes are evaluated in a gas diffusion electrode (GDE) half-cell, where an optimized catalyst layer composition leads to significantly improved ORR performance. By fine-tuning both the α-MnO$_2$-to-Vulcan ratio and the α-MnO$_2$ loading, the electrode outperforms a commercial MnO$_2$-based electrode and approaches the performance of the Pt/C benchmark. The improvement is attributed to the presence of a three-dimensional (3D) Vulcan network electronically connecting catalytically active α-MnO$_2$ sites with the substrate. Additionally, the optimized electrodes are employed in a prototype Al-O$_2$ flow cell. Under constant oxygen flow, power densities exceed 250 mW cm^{-2}, which is significantly higher than that of conventional Al-air batteries. Electrochemical impedance spectroscopy combined with distribution of relaxation times (DRT) analysis enables the separation of anode and cathode charge transfer impedances without the need for an additional reference electrode. The analysis reveals that the anode contributes more than twice as much impedance as the cathode, highlighting the need for further anode optimization. This work demonstrates a transferable approach for catalyst layer screening under technically relevant conditions in the GDE half-cell. Subsequent measurements in an Al-O$_2$ flow cell validate the approach. The methodology is widely applicable to the development of advanced electrodes for a variety of metal-air battery technologies.

© 2025 The Authors. Published by Published by Elsevier B.V. and Science Press on behalf of Science Press and Dalian Institute of Chemical Physics, Chinese Academy of Sciences. This is an open access article under the CC BY license (http://creativecommons.org/licenses/by/4.0/).

1. Introduction

The oxygen reduction reaction (ORR) in alkaline media is a key process for metal-air batteries, with aluminum-air (Al-air) batteries standing out as an up-and-coming technology for cost-effective and CO$_2$-free long-term energy storage. This promise arises from very high theoretical specific capacity (2980 mAh g^{-1}) and gravimetric energy density (8100 Wh kg^{-1}) of Al, along with its abundance, safety, and ease of handling [1–6]. Furthermore, although Al-air batteries are non-rechargeable, a closed CO$_2$-free Al cycle can be realized by recycling the discharge product (Al hydroxide) through inert-anode smelting, making this system highly attractive for sustainable large-scale applications [7–9].

Despite these advantages, the widespread implementation of Al-air batteries is still limited by significant activation losses at both electrodes, which drastically reduce their practical performance compared to theoretical values.

This study addresses the optimization of the cathode, where the ORR takes place and large overpotentials are observed. While Pt is widely regarded as the benchmark ORR catalyst [10], it suffers from high cost, scarcity, and potential fading in highly alkaline environments [11,12]. In contrast, manganese oxides, particularly the α-MnO$_2$ phase, offer a low-cost alternative with notable ORR activity [13–16]. Additionally, there are many facile and scalable synthesis routes available, such as several one-pot syntheses via acid-digestion [17–19] or ultra-fast microwave-assisted syntheses [20–22]. α-MnO$_2$ contains an open crystal tunnel structure that facilitates ion transport [13]. Additionally, α-MnO$_2$ contains more oxygen vacancies than other phases, leading to an accumulation

---

of electrons at these defect sites [23]. This results in a high adsorption energy of *OOH, *O, and *OH, and an improved electronic conductivity, which promotes the ORR [24,25]. However, its intrinsically low electronic conductivity remains the key bottleneck, limiting its practical use as an ORR catalyst [25,26].

Several strategies have been proposed to overcome this limitation, such as doping or coating α-MnO$_2$ with conductive species [27–34]. While effective, these approaches introduce additional synthesis steps, which increase cost and complexity and raise concerns about long-term stability. The central challenge is therefore to boost α-MnO$_2$ conductivity and performance using methods that remain both simple and scalable.

In this work, we address this challenge by optimizing the physical mixing ratio of α-MnO$_2$ and Vulcan-XC72R, a widely used conductive catalyst support known for its high conductivity, large surface area, and chemical stability in alkaline media, particularly when elevated potentials are avoided [10,35,36]. By systematically varying the α-MnO$_2$-to-Vulcan ratio, we identify the optimal catalyst layer composition that maximizes performance while avoiding additional synthesis complexity. To accelerate this optimization, we employ a gas diffusion electrode (GDE) half-cell, which enables testing under technically relevant conditions such as high current densities, highly alkaline molarities, and elevated temperatures.

The optimized electrodes are subsequently tested in a prototype Al-O$_2$ flow cell to validate their performance under full-cell conditions. Similar to a hydrogen fuel cell, oxygen is introduced instead of air to achieve higher performance. To gain further insights, electrochemical impedance spectroscopy (EIS) is combined with the distribution of relaxation times (DRT) analysis. DRT provides a powerful way to separate impedance contributions based on time regimes without the need for a priori knowledge of the system [37,38]. While DRT has been applied to other metal-air systems such as Zn-air [39], Li-O$_2$ [40–43], and Na-O$_2$ batteries [44,45], and also on the ORR in the GDE half-cell [11] and in the rotating disk electrode [46]; to our knowledge, this is the first application to Al-O$_2$ batteries.

Overall, this study introduces a simple yet effective strategy to enhance the ORR performance of α-MnO$_2$ through optimized incorporation with a conductive support, while demonstrating a combined GDE/full-cell procedure that enables rapid electrode screening under realistic conditions. This approach is easily transferable to other metal-air battery systems.

2. Experimental

All chemicals used in this work were used as received without further purification. Ultrapure water (0.055 μS) from the water dispenser PURELAB®flex (Elga) was used for the syntheses, preparing the KOH solutions, and cleaning. All potentials in this study are given against the reversible hydrogen electrode (RHE). Further experimental details not included in the Experimental Section can be found in the Supporting Information.

2.1. Synthesis of α-MnO$_2$

The synthesis of α-MnO$_2$ through acid digestion is an established and scalable synthesis route, which involves the disproportionation of Mn(III) into Mn(IV) and soluble Mn(II) [17,47,48]. 5.5 g of Mn$_2$O$_3$ (Sigma-Aldrich, 99%) were added to 300 mL of 6 M sulfuric acid (Thermo Scientific, 96%). The solution was heated to 130 °C and stirred for 16 h. The black product was filtered, washed with ethanol and ultrapure water, and dried.

2.2. GDE fabrication

The gas diffusion electrodes (GDE) consist of a gas diffusion layer (GDL) with a microporous layer (MPL, Freudenberg H23 C2)

and a catalyst layer (CL) on top. The CL was applied via spray coating with an airbrush system. The ink was prepared by adding respective amounts of the synthesized α-MnO$_2$ catalyst and either Vulcan XC-72R (FuelCellStore) or Ketjenblack EC-600JD (Nanografi) to 4 mL of ultrapure water and 4 mL of isopropanol. The dispersion was homogenized for 30 min in an ultrasonic bath. A respective amount of a 60 wt% polytetrafluoroethylene (PTFE) dispersion in water (Sigma-Aldrich) was added, and the ink was further homogenized with a tip sonicator for 30 s. During spray-coating, the GDL was placed on a heating plate at 80 °C to remove all volatile substances. Between each spray, the ink was placed in the ultrasonic bath. Electrodes with different α-MnO$_2$-to-Vulcan ratios and α-MnO$_2$ loadings were prepared. If not stated otherwise, the PTFE amount is 5 wt% in the dry CL. The benchmark electrode was prepared with 60% platinum on high-surface-area advanced carbon support (Thermo Scientific), without mixing it with additional Vulcan. The commercial manganese dioxide electrode (MOC air electrode with a PTFE layer, Gaskatel) consists of ca. 6 mg cm^{-2} manganese dioxide and ca. 10 mg cm^{-2} carbon, with PTFE as a binder. The catalyst layer is applied on a thin gas-permeable PTFE layer. A nickel mesh, as the current collector, is located on top of the catalyst layer. After thorough cleaning, the same nickel mesh was used for some measurements with the self-fabricated electrodes by placing it on the catalyst layer.

2.3. Half-cell measurements

Half-cell measurements were performed with a Zennium potentiostat (Zahner Elektrik) in a commercial GDE half-cell (Flex-Cell® PTFE, Gaskatel). The geometrical active surface area, which is defined by silicone sealings, is 3 cm^2. The cell is heated to 50 °C by PTC heating elements, which are connected to a temperature control box (Gaskatel). The reference electrode is an RHE Mini-HydroFlex (Gaskatel), and the counter electrode consists of a platinum-iridium wire. 4 M KOH (Emplura®, Merck) electrolyte was used for all measurements. Prior to a measurement, the electrolyte was purged with gas (nitrogen or oxygen) for 45 min to ensure complete saturation with the respective gas. A detailed overview of the measurement protocol can be found in our previous publication [11]. The GDE half-cell measurements were post-corrected using the uncompensated resistance. The ohmic resistance was determined using EIS by taking the real part of the resistance at the high-frequency intercept on the *x*-axis of the Nyquist plot. The reproducibility of the GDE half-cell measurements is demonstrated in Fig. S1.

2.4. Al-O$_2$ cell measurements

An in-house built Al-O$_2$ flow cell was operated with a Zennium Pro potentiostat (Zahner Elektrik) in an oven (Heratherm, Thermo Scientific) at 50 °C. The cell is a further development of the prototype cell used by Xu et al. [9] and is made of PTFE. An overview of the cell and its connecting parts is displayed in Fig. S2. The geometrical active surface areas of both electrodes were fixed to 0.95 cm^2. The cathode-to-anode distance was reduced to 5 mm to decrease the electrolyte resistance. Instead of an open shape on the outside of the cathode side, the new version has a closed casing with gas tube connections. This enables measurements at higher currents and, consequently, at high power due to the use of pure oxygen. The measurements were performed under an oxygen flow of 100 mL min^{-1} at 1.0 bar. An aluminum plate (99.997%, 1.0 mm thick, Thermo Scientific) was employed as the anode. A separate electrolyte tank connected to the cell by silicone tubing contained 40 mL of 4 M KOH with 5 g L^{-1} Na$_2$SnO$_3$·3H$_2$O (95%, Sigma-Aldrich) to suppress the aluminum self-corrosion [49]. The electrolyte was pumped through the cell between the two electrodes with a peri-

staltic pump (Masterflex L/S, Cole-Parmer) at a flow rate of 5 mL min^{-1}. Polarization curves were measured in galvanostatic steps of 1 min per step. The error bars are based on the standard deviation at each step. The average voltage, coulombic efficiency (CE), and specific energy (SE) for the aluminum anode were determined using a two-hour galvanostatic measurement at 100 mA cm^{-2}. After the measurement, the aluminum anode was carefully cleaned with ultrapure water to remove all precipitates and then dried at 80 °C. The aluminum anode was weighed before and after the two-hour experiment to calculate the aluminum consumption.

2.5. Electrochemical impedance spectroscopy

Electrochemical impedance spectroscopy (EIS) measurements were performed identically for the GDE half-cell and the Al-O$_2$ cell. Galvanostatic EIS measurements over the frequency range from 100 kHz to 100 mHz were carried out at 100 mA cm^{-2} with an alternating current (AC) of 10 mA. Clear outliers were removed to provide high-quality data for further processing. The distribution of relaxation times (DRT) analysis was used to evaluate the data further. The DRT transformation was conducted via the ec-idea software, which is also applicable to inductive contributions [50]. A regularization parameter of 0.5 was chosen. This value was determined in our previous work to best fit the system [11].

3. Results and discussion

3.1. Characterization of α-MnO$_2$

The synthesis of α-MnO$_2$ by acid digestion is a facile, inexpensive, and scalable process. By carefully adjusting conditions such as temperature, time, and pH, the desired phase of the manganese dioxide can be achieved. At low pH and elevated temperatures, the α-phase is formed [17]. In Fig. 1(a, b), scanning electron microscope (SEM) micrographs show the typical rod structure of α-MnO$_2$. Although there exist some other morphologies of α-MnO$_2$, the typical one-dimensional (1D) material, a rod or wire shape, is the most common [13,14]. The SEM images show a uniform distribution of the nanoparticles in shape and size. The rod-shaped nanoparticles have a thickness of 20–40 nm and a length of less than 400 nm (Fig. S3). The high-angle annular dark-field scanning transmission electron microscopy (HAADF-STEM) image of individual nanorods in Fig. 1(c), together with the energy dispersive

Fig. 1. (a, b) SEM images of α-MnO$_2$. (c) HAADF-STEM image of single α-MnO$_2$ particles and corresponding EDX elemental maps for (d) manganese (Mn) and (e) oxygen (O).

X-ray spectroscopy (EDX) elemental maps, displays a homogeneous distribution of both elements along the particles.

The X-ray diffraction (XRD) pattern in Fig. 2(a) reveals a pure tetragonal phase of the α-phase of the as-prepared manganese dioxide. The lattice constants are $a = b = 0.9840$ nm and $c = 0.2861$ nm, which differ from the literature regarding the a and b axes (PDF #44-0141, $a = b = 0.9785$ nm and $c = 0.2863$ nm). This can be explained by loosened lattice constraints in the nanostructure and differences in the growth orientation [51]. Furthermore, no signals from the precursor Mn$_2$O$_3$ can be detected. The thermogravimetric analysis (TGA) curve measured under an oxygen atmosphere in Fig. 2(b) demonstrates an initial decrease in catalyst weight of about 6 wt% up to 400 °C. In this temperature range, the α-MnO$_2$ loses first surface water and then crystal water. At higher temperatures above 500 °C, the conversion to Mn$_2$O$_3$ occurs [52]. However, the TGA curve indicates two decomposition stages, which are more clearly visible in the derived thermogravimetric analysis (DTG) curve with its two distinct peaks. A previous study using high-temperature XRD on α-MnO$_2$ suggested that the reaction first proceeds partially to Mn$_3$O$_4$, followed by decomposition to Mn$_2$O$_3$ [53]. The TGA and DTG results indicate a high thermal stability of α-MnO$_2$. The samples characterized by dynamic vapor sorption (DVS) measurements correspond to the catalyst layers studied later in the GDE half-cell. Different α-MnO$_2$-to-Vulcan ratios with 5 wt% PTFE in the powder are investigated, and the DVS isotherms are shown in Fig. S4. Low ratios of α-MnO$_2$ indicate a type V isotherm, which is characteristic of weak gas-adsorbent interaction and strong intermolecular gas interaction. Hydrophobic substances, such as non-polar carbon black, typically exhibit such behavior [54]. With increasing α-MnO$_2$ share, the adsorption isotherm evolves into a type IV isotherm. α-MnO$_2$, as an oxide, has a polar surface and therefore shows a stronger interaction with water. The hysteresis between the adsorption and desorption curves at higher relative humidities (RH) can be explained by the presence of an extensive pore network, which is more pronounced in samples with higher Vulcan ratios. The adsorption isotherm values at 20% RH are displayed in Fig. 2(c). At 20% RH, the pore filling and the water-water interactions are not yet pronounced, allowing the pure surface polarity to be studied. An almost linear decrease in water sorption is obtained by increasing the Vulcan ratio. A more hydrophobic catalyst layer has been shown to improve the ORR performance, particularly at high currents, due to enhanced gas transport [55,56]. However, the hydrophobic/hydrophilic microenvironment of the catalyst directly influences the triple phase boundary, thereby affecting many different processes. It must therefore be precisely tuned for each system [57]. A significant drawback of α-MnO$_2$ is its low electronic conductivity. The electronic conductivity of the as-prepared α-MnO$_2$ was measured with a special torque cell, schematically displayed in Fig. 2(d), and has a value of 0.036±0.009 S m^{-1}. This value is consistent with previously reported values for α-MnO$_2$ of 0.0045–0.0366 S m^{-1} [25]. It is significantly higher than many other manganese oxides and corresponds to semiconductor conductivities [25,26]. In comparison, Vulcan-XC72R, used as the catalyst support material, has an electronic conductivity of 277 S m^{-1} [35], which is four orders of magnitude higher. Tailoring the catalyst layer by adjusting the catalyst and support material ratio is a cost-effective approach to improving the overall conductivity of the catalyst layer and thus enhancing the ORR performance. Unlike other studies, no additional syntheses or the introduction of new materials are required. Different from conductive coatings or modifications on the α-MnO$_2$ surface, which tend to dissolve or rearrange over time, Vulcan XC-72R is expected to be stable.

Fig. 3 shows the segmented SEM images of electrodes with different α-MnO$_2$-to-Vulcan ratios. The blank version is illustrated in
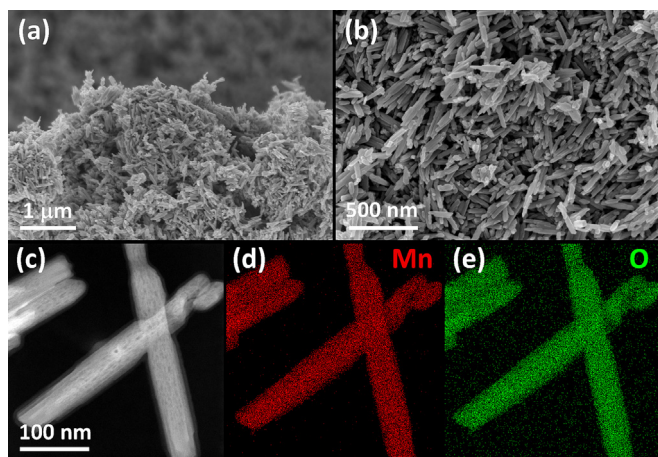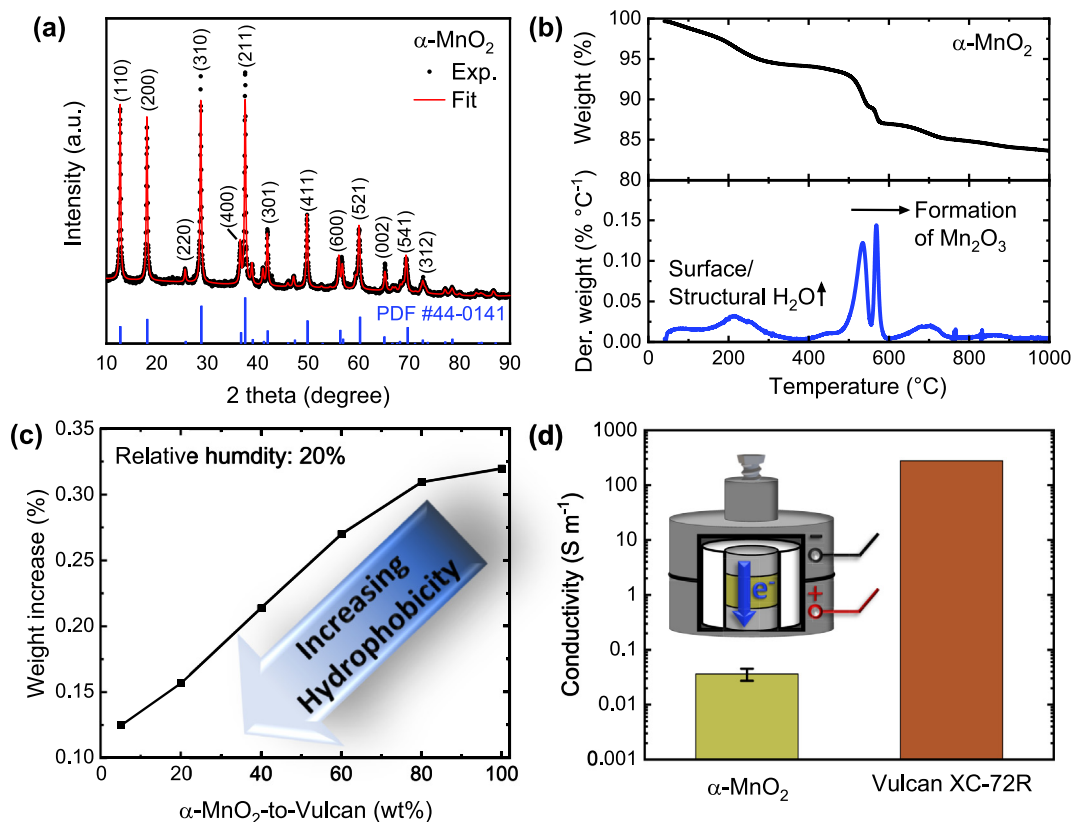
Fig. 2. (a) Indexed XRD pattern with fit result of α-MnO$_2$. (b) TGA and DTG curves of α-MnO$_2$. (c) DVS measurements of various α-MnO$_2$-to-Vulcan ratios and a PTFE content of 5 wt%. (d) The conductivity results of α-MnO$_2$ measured with a torque cell (schematic illustration) and of Vulcan XC-72R taken from the literature [35].

Fig. S5. The segmentation allows the visualization of the distribution of the catalyst and catalyst support material within the catalyst layer. In Fig. 3(f), which depicts an α-MnO$_2$ ratio of 100%, only nanorods can be detected. Proceeding from Fig. 3(f) to Fig. 3(a), the area corresponding to α-MnO$_2$ decreases, while the regions assigned to Vulcan increase. This is consistent with the designated ratios. 80% α-MnO$_2$/C demonstrates large agglomerations of α-

MnO$_2$, while 40% and 60% contain clusters, in which not all nanorods are in direct contact with Vulcan. Conversely, 5% and 20% α-MnO$_2$/C predominantly display single particles surrounded by Vulcan. This trend can also be followed in Fig. S6, in which the pixel share of the assigned areas is plotted against the α-MnO$_2$-to-Vulcan ratio. It is remarkable that the α-MnO$_2$ pixel share is halved going from 100% α-MnO$_2$ to 80% α-MnO$_2$/C. The entire curve
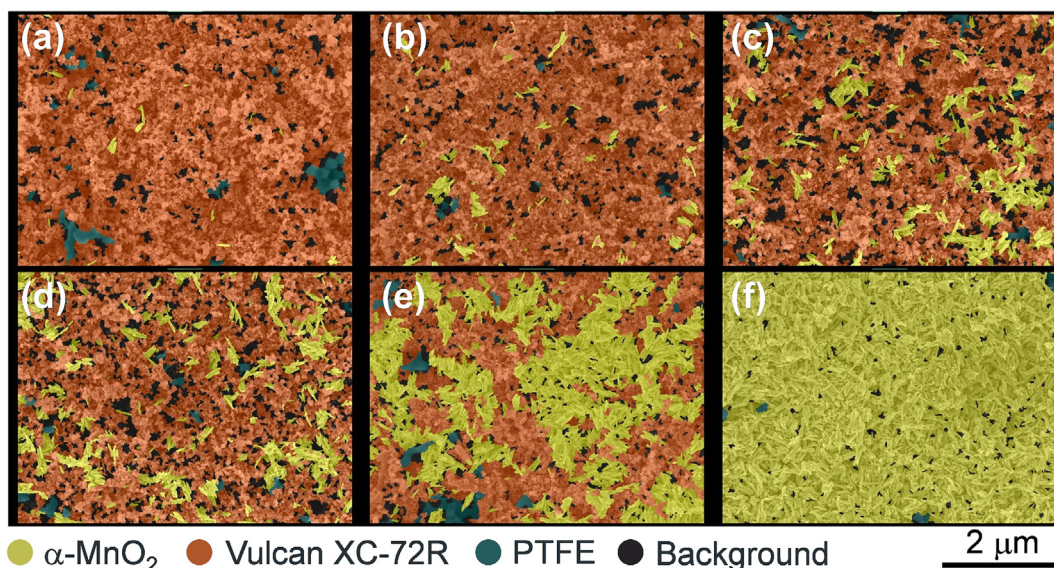
Fig. 3. Segmented SEM images to visualize the distribution of α-MnO$_2$ and Vulcan in the electrodes. GDEs with the following α-MnO$_2$-to-Vulcan ratios within the catalyst layer are shown: (a) 5%, (b) 20%, (c) 40%, (d) 60%, (e) 80%, and (f) 100%. All catalyst layers contain 5 wt% of PTFE.

resembles that of an exponential decay. This observation can be attributed to the significantly different specific surface areas of α-MnO$_2$ and Vulcan, which are 31 and 231 m^2 g^{-1}, respectively (Fig. S7). Given the poor electronic conductivity of α-MnO$_2$, it is crucial to optimize the local catalyst environment. A catalyst nanoparticle that is fully embedded in the conductive support material has improved access to electrons, a pivotal factor in electrochemical reactions. Therefore, from an electronic conductivity perspective, the 5% and 20% α-MnO$_2$/C are expected to show an enhanced ORR performance.

3.2. Optimization of α-MnO$_2$ electrodes in a GDE half-cell

The DVS measurements in Fig. 2(c) show that by altering the α-MnO$_2$-to-Vulcan ratio, the hydrophobicity of the catalyst layer can be modified. However, the ratio also affects many other parameters, such as the local catalyst environment, the catalyst layer thickness, and the electronic conductivity. To overcome these interdependencies, the hydrophilicity/hydrophobicity of the catalyst layer is fine-tuned by adjusting the PTFE content. Fig. S8(a) depicts polarization curves of electrodes with varying PTFE contents measured with a GDE half-cell. This half-cell allows for technical conditions such as high current densities, elevated temperatures, harsh alkaline conditions, and the presence of the triple phase boundary. The conditions are nearly identical to those found in metal-air batteries and alkaline fuel cells. The electrode containing 5 wt% PTFE in the catalyst layer demonstrates the highest ORR potentials. A lower or higher PTFE amount leads to decreased performance. In addition to the polarization curve, EIS measurements were performed. The DRT analysis, an alternative evaluation method to equivalent circuit fitting, reveals an increased frequency of the charge transfer with greater PTFE content in the catalyst layer (Fig. S8b). The accelerated charge transfer process can be attributed to the augmented oxygen content near the catalyst, a consequence of the increased hydrophobicity. The charge transfer impedance is four times higher for 1 wt% PTFE than for the other electrodes. A deficiency in PTFE content within the catalyst layer can result in electrolyte flooding. This can prevent the oxygen from reaching many catalytically active sites, and thus, no triple phase boundary can be established. In contrast, more PTFE has little effect on the charge transfer impedance, but covers active catalytic sites, resulting in a diminished ORR performance. Interestingly, 5 wt% PTFE has also been reported to be the optimal amount for high-temperature proton exchange membrane fuel cell (PEMFC) using phosphoric acid in the membrane [58]. For the following electrodes, the PTFE content is maintained at 5 wt%.

Fig. 4(a) depicts the polarization curves of different α-MnO$_2$-to-Vulcan ratios. The α-MnO$_2$ loading is kept at 0.3 mg cm^{-2} to solely study the impact of the altered local catalyst environment and its influence on the performance of the electrode. The polarization curve of the pure α-MnO$_2$ catalyst layer shows the lowest ORR potentials. 80% α-MnO$_2$/C already exhibits significantly increased potentials, particularly at low current densities, as can be seen from the logarithmic representation in Fig. 4(b). This finding aligns with the previous observation of the segmented SEM images in Fig. 3(e, f), where the α-MnO$_2$ pixel share drastically decreases due to the introduction of Vulcan, explained by the substantial difference in specific surface area and thus density. Presumably, the introduction of small amounts of conductive catalyst support material enables an increased share of the present α-MnO$_2$ to participate as catalytic sites in the ORR. For the pure α-MnO$_2$ electrode, it can be assumed that almost exclusively the α-MnO$_2$ nanorods in direct contact with the substrate take part in the ORR. The polarization curves of 40% and 60% α-MnO$_2$/C demonstrate increased potentials, especially in the current density range of 1–100 mA cm^{-2}. However, at higher currents, the polarization

curves approach each other again. This potential fading cannot be explained by different ohmic resistances since all measurements in Fig. 4 are iR corrected. It also cannot be attributed to the lack of additional ORR activity of Vulcan. Although Vulcan has a specific intrinsic ORR activity in alkaline media, it does not achieve potentials as high as those observed here (Fig. S9). The observation is most likely due to α-MnO$_2$ particles that are not in contact with conductive Vulcan, and thus cannot participate in the reaction. At low currents, there are enough active sites with direct access to the support material. However, at high currents, a bottleneck is reached, leading to a reduction in potential. In contrast, 20% and 5% α-MnO$_2$/C exhibit remarkably increased potentials. In comparison to the previous electrodes, nothing indicates mass transport limitations. This is particularly evident in the logarithmic representation, where the 5% and 20% α-MnO$_2$/C electrodes show an almost constant slope, while the slope of the other electrodes starts to change at 1–10 mA cm^{-2}. The current density and the mass-normalized current at 0.85 V are illustrated in Fig. 4(c). Between 20% and 40% α-MnO$_2$/C, a substantial rise can be seen with more than double the current densities. The considerable impact is attributed to the strongly increased number of catalyst particles participating in the ORR. Nearly all of the α-MnO$_2$ nanorods in the 5% and 20% α-MnO$_2$/C electrodes are fully surrounded by Vulcan and do not tend to form large agglomerates or clusters (Fig. 3a, b). Furthermore, the described distribution of α-MnO$_2$ and Vulcan is not only representative of the electrode surface but is also expected to be similar in a three-dimensional perspective. Therefore, electrodes with 40% or more α-MnO$_2$/C may have an additional factor that impedes the ORR. α-MnO$_2$ particles in these electrodes, although being in contact with Vulcan, may not have direct electron channels consisting of conductive Vulcan to the substrate. Instead, the channels may be blocked by α-MnO$_2$ agglomerates located deeper in the catalyst layer. The 5% and 20% α-MnO$_2$/C electrodes appear free of these limitations, reaching their full intrinsic activity.

The above explanation can be further confirmed by replacing the catalyst support material Vulcan (VC) with Ketjenblack (KB). KB possesses similar properties to VC but features a higher specific surface area. Consequently, the threshold at which the α-MnO$_2$ becomes well dispersed and its intrinsic ORR performance is achieved must be at a higher α-MnO$_2$-to-C ratio. As shown in Fig. S10, the 40% α-MnO$_2$/KB electrode already exhibits nearly optimal ORR performance, comparable to the 20% α-MnO$_2$/VC electrode, and reaches identical performances at 20% α-MnO$_2$/KB. Nevertheless, the present work focuses on Vulcan as support material since it is more cost-effective, yields comparable results, and is therefore of greater technical relevance.

The 5% and 20% α-MnO$_2$/C electrodes display a very similar ORR performance with almost identical polarization curves (Fig. 3a, b). They only differ in the highest current point, with the 5% electrode slightly outperforming the 20% electrode. However, the thick catalyst layer of the 5% α-MnO$_2$/C electrode, which contains nearly five times more Vulcan, lacks mechanical stability, and after the measurement, particles floated in the electrolyte. Thus, no stable signal could be detected during the EIS measurement.

The Nyquist plots of all other electrodes are presented in Fig. 5 (a). The curves are very similar except for 20% α-MnO$_2$/C, which exhibits a significantly reduced semicircle. In addition, the Nyquist plots of 40%–80% α-MnO$_2$/C show a pseudo-inductive behavior at low frequencies. Such behavior has been previously reported for fuel cells and attributed to the slow removal of site-blocking species from the cathode surface [59–61]. The evaluation of the EIS results using DRT analysis allows for the separation of individual processes based on the time regime. The DRT plot in Fig. 5(b) unveils a significant peak for every electrode. Since the measurements were performed at moderate current densities of
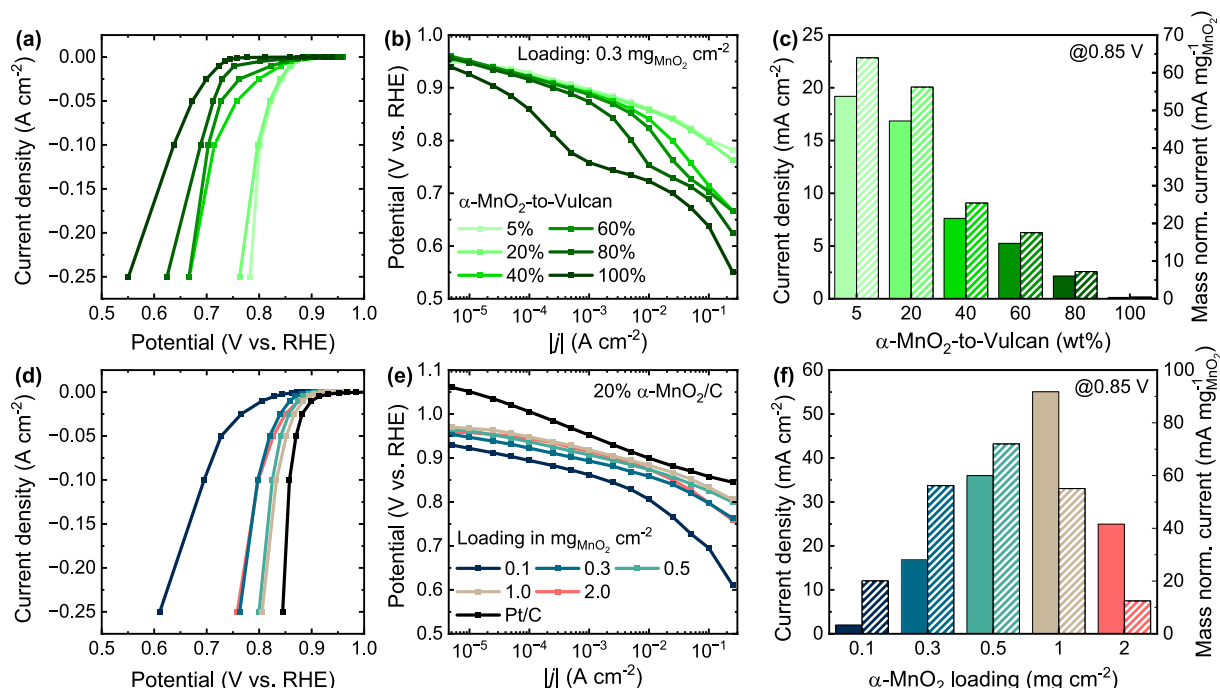
Fig. 4. (a, d) Polarization curve. (b, e) Corresponding logarithmic representation. (c, f) Current density and mass-normalized current density at 0.85 V. (a–c) corresponds to different α-MnO$_2$-to-Vulcan ratios implemented into a GDE. α-MnO$_2$ loading is fixed to 0.3 mg cm^{-2}. (d–f) corresponds to 20% α-MnO$_2$/C implemented into a GDE with different α-MnO$_2$ loadings. Pt/C benchmark has a platinum loading of 0.3 mg cm^{-2}. Measurements were performed in the GDE half-cell at 50 °C in 4.0 M KOH. All values are *iR* corrected.
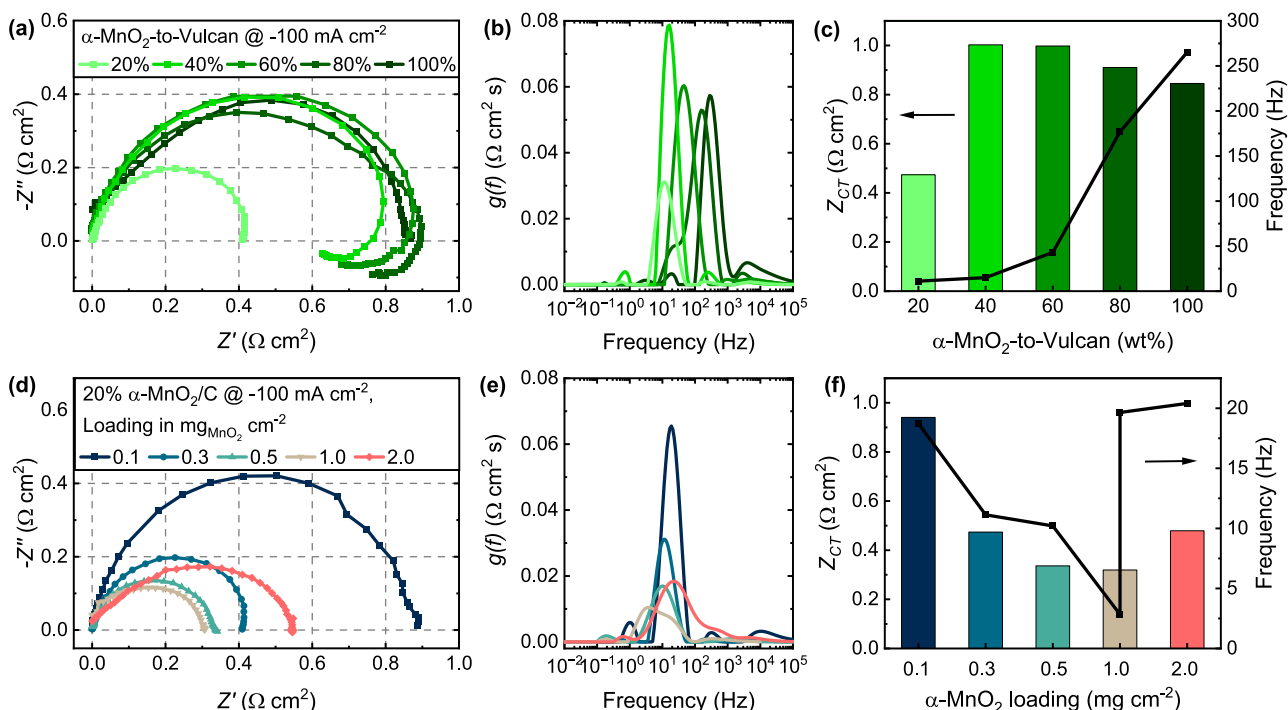
Fig. 5. (a, d) *iR* corrected Nyquist plot. (b, e) DRT plot. (c, f) Charge transfer impedance contribution and frequency determined from the DRT analysis. (a–c) corresponds to different α-MnO$_2$-to-Vulcan ratios implemented into a GDE. α-MnO$_2$ loading is fixed to 0.3 mg cm^{-2}. (d–f) corresponds to 20% α-MnO$_2$/C implemented into a GDE with different α-MnO$_2$ loadings. Measurements were performed in the GDE half-cell at 50 °C in 4.0 M KOH.

100 mA cm^{-2} under oxygen excess and with no expected anode contribution, this peak can be attributed to the charge transfer of the ORR. Furthermore, in our previous publication introducing DRT analysis for the GDE half-cell with Pt and Ag catalysts, the single prominent peak, which was assigned to the charge transfer of the ORR, is located in the same frequency range [11]. The prominent peak for 80% α-MnO$_2$/C indicates a shoulder towards lower frequencies. Most likely, the DRT analysis could not resolve the charge transfer process as a single peak since its time regime is broadened in that electrode. Fig. 5(c) displays the extracted values

from the DRT analysis. Going from 20% to 100% α-MnO$_2$/C, the frequency of the charge transfer increases from 11.1 to 265.3 Hz. This significant increase is attributed to the catalyst layer thickness. Since all electrodes have the same α-MnO$_2$ loading of 0.3 mg cm^{-2}, electrodes with high α-MnO$_2$-to-Vulcan ratios have thinner catalyst layers. Oxygen, therefore, is always available in the direct vicinity, and by that, ORR charge transfer is accelerated. Interestingly, the more hydrophobic nature of 20% α-MnO$_2$/C identified by the DVS measurement (Fig. 2c) does not affect the frequency of the charge transfer process. Hence, it does not seem to improve the oxygen availability, or its effect is outperformed by the catalyst layer thickness. The charge transfer impedance in Fig. 5(c) exhibits an increase from 0.845 to 1.003 Ω cm^2 from 100% to 40% α-MnO$_2$/C, while the 20% α-MnO$_2$/C has by far the lowest value of 0.474 Ω cm^2. Catalyst particles that are not in contact with Vulcan, and therefore not participating in the ORR, also do not contribute to the impedance. Thus, the slight increase from 100% to 40% α-MnO$_2$/C can be attributed to the thicker catalyst layer, which does not significantly improve the electronic conductivity of the catalyst layer. However, the lowest values of the 20% α-MnO$_2$/C can be explained by the presence of a 3D network of electron pathways consisting of conductive Vulcan within the catalyst layer connecting the catalysts with the substrate. This leads to a significant increase in conductivity of the overall catalyst layer and thus reduces the charge transfer impedance. The optimized 3D network is established somewhere between 20% and 40% α-MnO$_2$/C, and it is assumed that a threshold exists since the impact is so pronounced.

The 20% α-MnO$_2$/C demonstrates significantly improved ORR performance, and unlike the 5% α-MnO$_2$/C, it does not suffer from mechanical stability issues. Therefore, this ratio will be further studied by varying the α-MnO$_2$ loading from 0.1 to 2.0 mg cm^{-2}.

The polarization curves continuously shift to more positive potentials as the loading increases (Fig. 4d). The polarization curve corresponding to the 2.0 mg cm^{-2} loading deviates from the trend. It follows a similar curve representing the 0.3 mg cm^{-2} loading. The electrode with the 1.0 mg cm^{-2} loading shows the best ORR performance. Its potential at 100 mA cm^{-2} is improved by 36 mV compared to the previous electrode with a loading of 0.3 mg cm^{-2}, but it is still 25 mV behind the Pt/C electrode. This is a remarkable performance for a non-precious metal catalyst, considering that the Pt/C benchmark shown here is one of the best performing Pt/C catalysts in highly alkaline media [11]. Other Pt/C catalysts exhibit significant potential fading at high current densities [11,12]. The logarithmic representation in Fig. 4(e) shows relatively straight curves for 0.5 and 1.0 mg cm^{-2}, but apparent shifts in the slope of the curves for 0.1 and 2.0 mg cm^{-2}. Especially at high currents, a pronounced potential drop is visible, indicating mass transport limitations. For 0.1 mg cm^{-2}, this is attributed to the insufficient number of catalytic sites. Conversely, for 2.0 mg cm^{-2}, it is ascribed to the hindered oxygen supply due to the thick catalyst layer. The 0.5 and 1.0 mg cm^{-2} electrodes show similar ORR performance. However, at 0.85 V, the 1.0 mg cm^{-2} electrode shows a 50% higher current density of 55.1 mA cm^{-2}. In contrast, the 0.5 mg cm^{-2} electrode exhibits the highest mass-normalized current density of 72.0 mA mg$_{MnO_2}$$^{-1}$ (Fig. 4f). This means that the catalyst in the 0.5 mg cm^{-2} electrode catalyzes the ORR most efficiently. However, the mass-normalized current is not technically relevant because manganese dioxide is inexpensive compared to other ORR catalysts.

The Nyquist plots in Fig. 5(d) align well with the polarization curve results. The DRT plot reveals one prominent peak for all electrodes (Fig. 5e). This peak diminishes with increasing loading until 1.0 mg cm^{-2}, but its shape becomes broader at the same

time. At higher loadings, active sites with more diverse microenvironments are involved in the ORR since the catalyst layer is thicker. Catalysts closer to the electrolyte have different access to oxygen and electrolyte compared to those closer to the substrate. This results in the broader velocity range of the ORR charge transfer. Fig. 5(f) summarizes the extraction of the charge transfer impedance and its frequency. The charge transfer impedance displays a similar trend to the polarization curve, with the lowest value of 0.320 Ω cm^2 at 1.0 mg cm^{-2}. More catalytically active sites significantly reduce the charge transfer impedance. However, the 2.0 mg cm^{-2} shows an increased impedance value of 0.479 Ω cm^2, indicating a reduced number of sites involved since some sites are no longer supplied with oxygen. The frequency also supports this conclusion. From low to high loading, it first decreases due to the thicker catalyst layer and therefore reduced local oxygen availability. At 1.0 mg cm^{-2}, two convoluted peaks appear in the DRT plot, instead of an expected single broad peak. This may be due to the DRT algorithm trying to introduce more peaks. However, catalytic sites closer to the substrate are expected to show a faster charge transfer, while sites farther away exhibit slower rates. Interestingly, main sites close to the substrate participate in the ORR for the 2.0 mg cm^{-2}. This is most likely because the catalysts farther away from the substrate are no longer supplied with oxygen, either due to electrolyte flooding or pore blocking.

The optimization of the α-MnO$_2$ catalyst layer by adjusting the α-MnO$_2$-to-Vulcan ratio and by fine-tuning the loading strongly improves the ORR performance. This is also evident when comparing it to the commercial MnO$_2$-based air electrode from the company Gaskatel. The polarization curves in Fig. S11(a) reveal a better performance of the 20% α-MnO$_2$/C with a loading of 0.3 mg$_{MnO_2}$ cm^{-2} at high current densities. However, the loading of the commercial electrode, with a value of ca. 6 mg$_{MnO_2}$ cm^{-2}, is significantly higher. The logarithmic representation in Fig. S11(b) allows a closer inspection. The onset potential is very similar at around 0.95 V. At low current densities, the commercial electrode displays higher potentials due to the increased number of active sites. However, at around 15 mA cm^{-2}, the situation reverses, exhibiting improved ORR performance for the 20% α-MnO$_2$/C. This is partly due to the high loading, which impedes the oxygen transport required at high currents. The main reason, however, is the suboptimal MnO$_2$-to-carbon ratio of about 38%, which leads to a pronounced potential fading at high current densities due to the low conductivity of the catalyst layer. As demonstrated here, it is essential to achieve the optimal ratio of catalyst to support material, especially in cases where the catalyst has low conductivity.

All measurements to this point have been *iR* corrected to investigate solely the catalyst layer performance. However, for full-cell measurements, the actual electrode performance is more relevant. The use of a nickel mesh as a current collector is a well-established technique since nickel is stable in alkaline conditions and has excellent electronic conductivity [62]. Electrochemical measurements with and without the nickel mesh are shown in Fig. 6. The Nyquist plot reveals an enormous shift in the semicircle position (Fig. 6a). The ohmic resistance decreases from 1.82 to 0.26 Ω cm^2 when using a current collector. The polarization curve in Fig. 6(b) shows a slight shift to lower potentials with the Ni mesh when the *iR* correction is applied. This is most likely attributed to some catalysts being covered by the Ni mesh. However, the electrode performance without any correction is significantly improved with the current collector. At 250 mA cm^{-2}, the electrode with the current collector has a potential more than 300 mV higher than the electrode without the nickel mesh. In the DRT plot (Fig. 6c), the
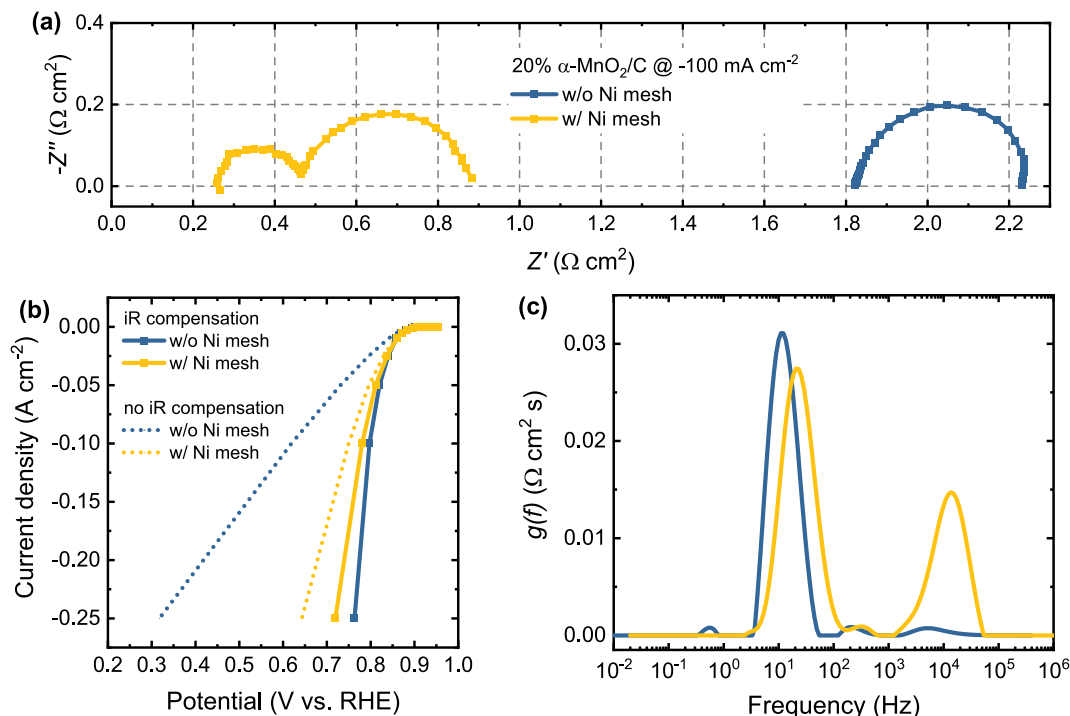
Fig. 6. (a) Nyquist plot at −100 mA cm⁻². (b) Polarization curve with (solid line) and without *iR* correction (dotted line). (c) DRT plot of the 20% α-MnO₂/C implemented into a GDE with and without a nickel mesh as current collector. Measurements were performed in the GDE half-cell at 50 °C in 4.0 M KOH.

electrode with Ni mesh has a much more pronounced high-frequency peak at about 15,000 Hz, indicating an impedance attributed to the additional electrical connection between the catalyst layer and the current collector.

3.3. Evaluation of α-MnO₂ electrodes in an Al-O₂ cell

The results of the GDE half-cell measurements are verified with an in-house-built Al-O₂ flow cell (Fig. S2). To prevent the hydrogen evolution reaction at the Al anode, sodium stannate, a corrosion inhibitor, was added to the electrolyte. To exclude any interaction of the additive on the cathode side, polarization curves with and without the additive were conducted in the GDE half-cell. The curves in Fig. S12 are nearly identical, and the minor shift can be attributed to the experimental error. This result confirms the absence of any cross-interaction of the additive on the cathode side.

A schematic illustration of an Al-air cell is displayed in Fig. 7(a). A tank of fresh electrolyte is required because $Al(OH)_4^-$ is formed during the electrochemical reaction, leading to a decrease in pH and cell performance over time. The Al products can be collected by extracting them from the electrolyte via seeded precipitation. By feeding those Al products into an inert-anode smelting process, Al can be recovered [9]. The combination of the primary Al-air battery and the external recovery of Al through inert-anode smelting is a potential option for cost-effective and zero-carbon-emission seasonal/annual energy storage [2]. To expand the Al-air cell to high-power applications, the cathode side in this work is purged with oxygen in the same manner as in the GDE half-cell and similarly to hydrogen fuel cells. This allows for a sufficient supply of the electrochemically active species even at high current densities. For clarity, the oxygen-purged Al-air cell is referred to as the Al-O₂ cell.

The open-circuit voltages (OCVs) of the Al-O₂ cell, summarized in Fig. S13, are approximately 1.90 V for the MnO₂-based electrodes and 1.96 V for Pt/C. The observed shift of more than

60 mV arises from the difference in ORR activity between MnO₂ and Pt. Fig. 7(b) shows the polarization curve of the 20% α-MnO₂/C cathode in comparison to the benchmark Pt/C and the commercial MnO₂-based electrode. Similar to the GDE half-cell measurements, the commercial electrode initially exhibits a curve equivalent to that of the 20% α-MnO₂/C electrode. However, the slope starts to differ at current densities greater than 50 mA cm⁻². The Pt/C electrode displays a clear gap to the 20% α-MnO₂/C electrode. This is consistent with the results in Fig. 4(d) since the 20% α-MnO₂/C has only an α-MnO₂ loading of 0.3 mg cm⁻². The maximum power densities are 297.9, 257.5, and 225.7 mW cm⁻² for the Pt/C, 20% α-MnO₂/C, and the commercial electrode, respectively. These values are substantially higher than previous reports [63–66] and demonstrate that using oxygen can significantly improve the power density. Similar results can be achieved by increasing the surface roughness of Al [67] or by using anodes based on Al alloys [68].

The discharge curves in Fig. 7(c) at 100 mA cm⁻² show a similar trend to the polarization curves. The small voltage fluctuations of about 10 mV are coming from small oxygen bubbles, reducing the active anode area. Due to the small dimensions of the electrodes of 0.95 cm² and the short anode-cathode distance of about 5 mm, the fluctuations become visible. The average voltage, coulombic efficiency, and the specific energy of Al are calculated based on the discharge curves and are summarized in Fig. 7(d). After the electrochemical measurement, notable amounts of Al are consumed, and a dark gray deposition appears (Fig. S14). This deposition can be carefully removed with water. The results of the inductively coupled plasma optical emission spectroscopy (ICP-OES) indicate that the deposition mainly consists of the elements K, Al, and Sn. This corresponds to KOH residues, $Al(OH)_3$/$Al(OH)_4^-$ products, and the formation of a thin metallic tin layer. The tin layer prevents Al from direct contact with the electrolyte and thus suppresses the parasitic corrosion reaction [69]. The coulombic efficiency (CE) values of 94%–96% (Fig. 7d) confirm the successful suppression. The deviations between the values are
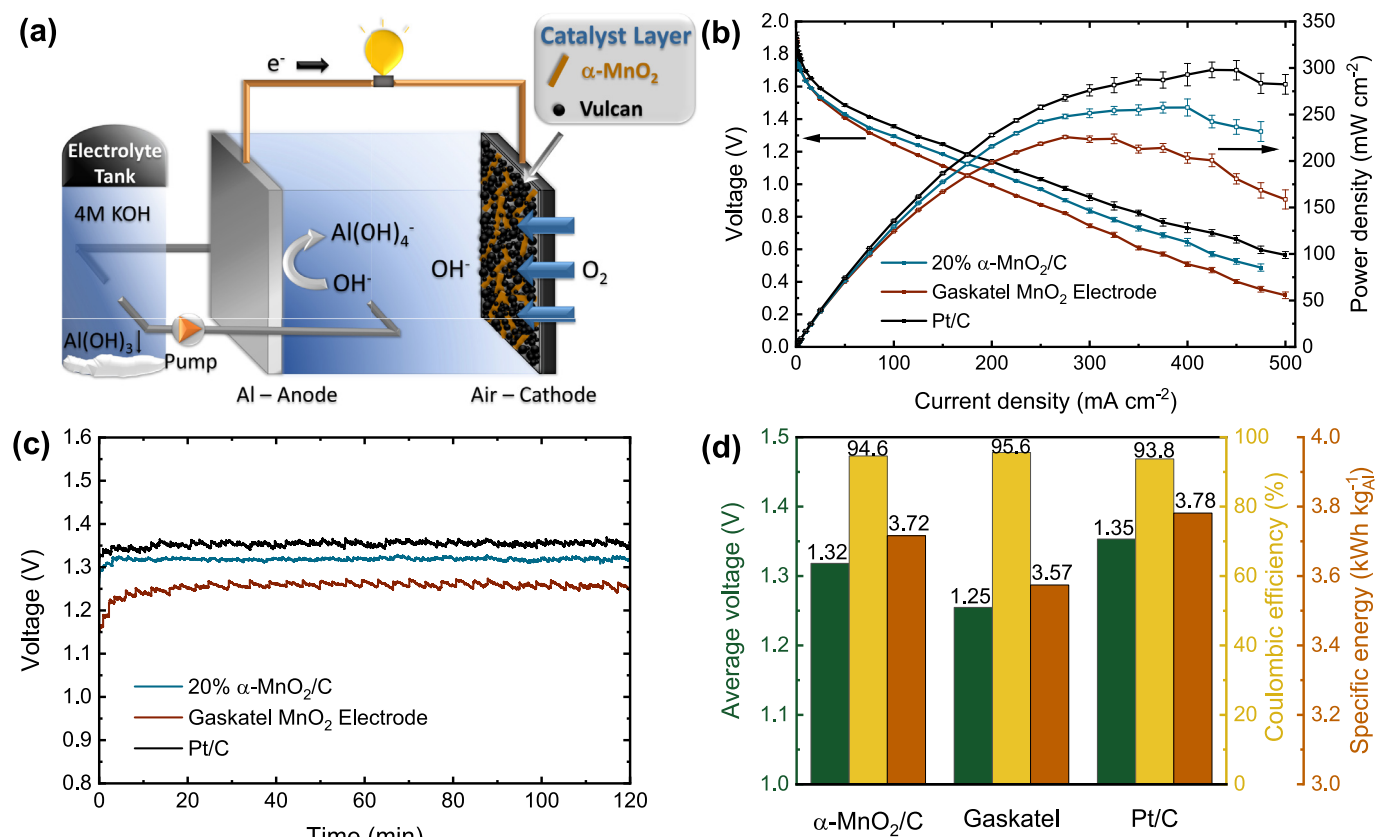
Fig. 7. (a) Schematic illustration of the Al-O_2 cell and the involved processes. (b) Polarization and power density curve. (c) Galvanostatic discharge curve at 100 mA cm^{-2}. (d) The corresponding average voltage, coulombic efficiency, and specific energy based on the aluminum anode for different cathodes with Ni mesh. α-MnO_2 and Pt loading are 0.3 mg cm^{-2}. Measurements were performed in an Al-O_2 flow cell at 50 °C.

minor and likely due to measurement errors since the Al anode and the electrolyte are identical for every measurement. The average voltage corresponding to the 20% α-MnO_2/C is only 30 mV lower than that of Pt/C and around 70 mV higher than the commercial electrode. The specific energy values of Al show improved results compared to many other publications, which have values far below 3.5 kWh kg$_{Al}^{-1}$ at 100 mA cm^{-2} [9]. This emphasizes the advantage of using an oxygen flow.

Cathodes with higher α-MnO_2 loading are also tested in the Al-O_2 cell since they show improved ORR performance in the GDE half-cell (see Fig. 4d). However, the polarization curves in Fig. S15(a) are almost identical. Also, the average voltage from the two-hour discharge measurement shows similar values of 1.31–1.32 V, indicating an almost identical performance of the cathodes in the Al-O_2 cell. A more detailed discussion and a possible explanation for that behavior are offered in the next section.

To study the different cathodes in more detail in the Al-O_2 cell, EIS measurements were performed and analyzed by DRT. As far as we know, this is the first time that DRT is used in the context of Al-air batteries. Therefore, EIS measurements were conducted at almost identical conditions in the GDE half-cell and the Al-O_2 cell to facilitate the peak assignment in the DRT plot. A comparable approach with a reference electrode was utilized by Bevilacqua et al. to identify the processes in the high-temperature polymer electrolyte membrane fuel cell [70].

Fig. 8(a) shows the Nyquist plots of 20% α-MnO_2/C with 0.3 mg cm^{-2} α-MnO_2 loading without a current collector in the GDE half-cell and Al-O_2 cell. Both measurements are performed at 50 °C with oxygen flow at the cathode in 4 M KOH with sodium stannate as the additive. Surprisingly, the ohmic resistance is very

similar at about 1.8 Ω cm^2, although the setups are different. The Nyquist plot corresponding to the Al-O_2 cell is more complex because it shows at least two pronounced semicircles instead of only one, as for the GDE half-cell. Similarly, the DRT plot in Fig. 8(b) reveals one major peak for the GDE half-cell and two significant peaks for the Al-O_2 cell. The first peak at 32 Hz shows a good overlap with the corresponding peak of the GDE half-cell. Therefore, it can be attributed to the charge transfer of the ORR. The slight shift towards higher frequency is most likely due to the flow conditions in the Al-O_2 cell, which may accelerate the product diffusion and thus the whole reaction. The corresponding ORR charge transfer impedance values listed in Fig. 8(c) are also similar. The impedance value is increased by 50 mΩ cm^2 for the Al-O_2 cell. The increase can also be attributed to the flow dynamics, which change the interphase among gas, liquid, and solid within the catalyst layer. This may lead to a reduced number of catalyst particles participating in the ORR. Another major peak in the DRT plot in Fig. 8(b) is located at 1673 Hz. Since this peak does not appear in the GDE half-cell, it must be attributed to the anode side, more precisely, to the aluminum oxidation charge transfer. The assignment will be further confirmed in the later discussion. The charge transfer impedance of the Al oxidation reaction is 0.990 Ω cm^2, more than double that of the ORR charge transfer impedance of 0.401 Ω cm^2. This agrees with a study of Wang et al., showing that the major overpotential contribution in an Al-air cell comes from the anode [71]. In the DRT plot, only one more little peak is visible at high frequencies, which can be assigned to the electrical connection of the cathode. This can be verified when comparing measurements with or without the Ni mesh in Fig. 6(c) and Fig. S16(c). The specific peak increases when using the Ni mesh since the electrons have an
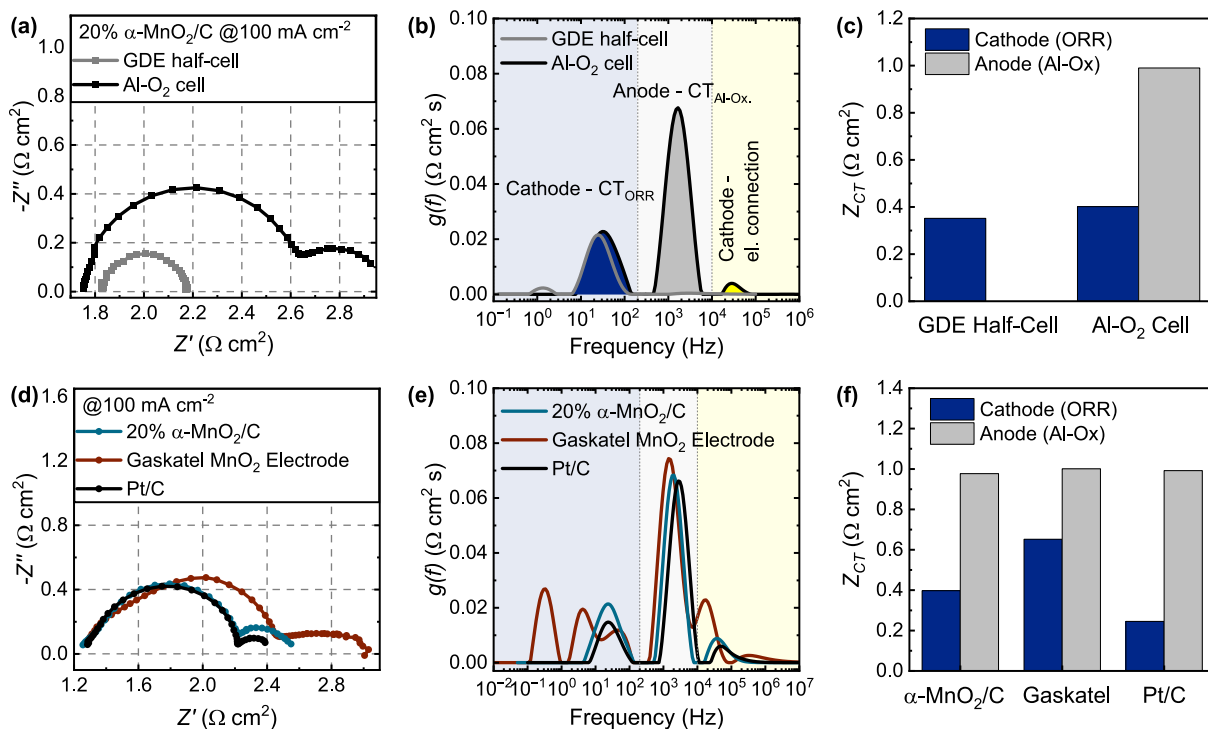
Fig. 8. (a, d) Nyquist plot. (b, e) DRT plot. (c, f) Charge transfer impedance contribution determined with DRT analysis. (a–c) The results are measured with the identical air electrode without Ni mesh in the GDE half-cell and the Al-O$_2$ flow cell at 50 °C in 4 M KOH and 5 g L^{-1} Na$_2$SnO$_3$·3H$_2$O. (d–f) corresponds to different cathodes with Ni mesh investigated in an Al-O$_2$ flow cell at 50 °C. α-MnO$_2$ and Pt loading are 0.3 mg cm^{-2}.

additional interface to overcome. Additionally, this assignment is supported by measurements at different currents (Fig. S17b). While all charge-transfer-related DRT peaks decrease with increasing current, as reported previously [11,72], the high-frequency peak even increases slightly. In the DRT plot (Fig. 8b), no mass-transport-related impedance can be detected (Fig. 8b) since the current density of 100 mA cm^{-2} is still moderate, particularly when the cathode is purged with oxygen. Furthermore, the polarization curves in Fig. 7(b) exhibit a constant slope over the entire current range except for the low current regime dominated by activation losses. This observation indicates the absence of any mass transport limitations. This is in accordance with a modeling study, which identified that the activation and ohmic overpotential are the major relevant factors for improving Al-air batteries [73].

Based on the general peak assignment in Fig. 8(b), it is possible to easily separate the impedance contributions of the electrodes without the need for an additional reference electrode. This reduces the complexity of the measurement setup and enables facile access to a deeper electrode performance analysis. Furthermore, the DRT assignment enables the appropriate selection of an equivalent circuit model that provides results comparable to those obtained from DRT analysis (Fig. S18 and Table S1). This alternative approach may be particularly useful for researchers who are not yet familiar with the DRT technique.

Fig. 8(d) displays the Nyquist plots corresponding to the previously compared cathodes in the Al-O$_2$ cell. The ohmic resistance is reduced to approximately 1.28 Ω cm^2 compared to 1.75 Ω cm^2 in Fig. 8(a) since the cathodes contain a Ni mesh. However, the ohmic resistance is still significant and should be further reduced when considering a technical application. The DRT plot in Fig. 8(e) reveals three peaks, except for the commercial MnO$_2$-based electrode, which exhibits two more peaks at low frequencies. The two additional peaks can be attributed to the ORR charge transfer resistance since they reduce in size when increasing the current

density—a typical indication for a charge-transfer-related peak [11,72]. The splitting of a single broad peak into multiple peaks is probably caused by the DRT algorithm [74]. The wide time regime can be explained by the high catalyst loading, which corresponds to a thick catalyst layer and catalyst sites with different microenvironments that exhibit different ORR velocities. Additionally, the only known information about the commercial electrode is that it is based on MnO$_2$. However, MnO$_2$ can occur in various phases with different ORR activities [14]. Therefore, the different time regimes may also originate from different crystal phases with different charge transfer frequencies. The evaluation of the DRT peaks in Fig. 8(f) displays ORR charge transfer impedance values of 0.397, 0.652, and 0.245 Ω cm^2 for the 20% α-MnO$_2$/C, the commercial electrode, and the Pt/C, respectively. These values fit well with the trend of the polarization curves in Fig. 7(b). However, the anode contribution remains relatively constant at about 1.0 Ω cm^2. This is also expected since the same aluminum anode and electrolyte are used for all experiments. With increasing performance of the Al-O$_2$ battery, the Al oxidation-related DRT peak in Fig. 8(e) shifts slightly toward higher frequencies, following the same trend as the cathode performance. Most likely, an improved ORR also slightly accelerates the processes of the whole cell and so also the Al oxidation.

The DRT plot of the 20% α-MnO$_2$/C cathodes with different α-MnO$_2$ loadings in the Al-O$_2$ cell is shown in Fig. S15(c). The peaks corresponding to the Al oxidation charge transfer and the electrical connection are similar. However, the peak attributed to the ORR charge transfer indicates a broadening from 0.3 to 0.5 mg cm^{-2}, and at 1.0 mg cm^{-2}, it splits up into two peaks. The integrated impedance values in Fig. S15(d) are still very similar and fit the identical polarization curves. Different from the GDE half-cell in Fig. 5(f), the ORR charge transfer impedance is not reduced with increased α-MnO$_2$ loading. The electrolyte flow dynamics seem to change the electrolyte/gas interphase and reduce the number

of participating catalysts in the ORR, thereby affecting the overall Al-O$_2$ cell performance. At static conditions, as found in the GDE half-cell, a thicker catalyst layer can be used since an improved interphase is established. To achieve static conditions for the cathode in the Al-O$_2$ flow cell, either a membrane must be used or a different cell architecture should be utilized. In the study by Wen et al. [68], an Al-air cell was used, with the electrolyte pumped through the backside of the Al anode. To allow for ion exchange, holes were drilled in the Al anode. Such a design creates quasi-static conditions at the cathode, enabling higher loading for improving the ORR. At the same time, a closer anode-to-cathode distance can be realized, reducing the ohmic resistance.

4. Conclusions

α-MnO$_2$ is a cost-effective ORR catalyst, but its low conductivity limits its performance. Here, we demonstrate that a simple optimization of the α-MnO$_2$-to-Vulcan ratio in the catalyst layer substantially enhances ORR performance, with 5% and 20% α-MnO$_2$/C electrodes achieving more than twice the current density of other ratios at 0.85 V. The improvement arises from a three-dimensional Vulcan network that enables efficient electron transport, allowing the catalyst to approach its intrinsic activity. At 1.0 mg cm^{-2} loading, the 20% α-MnO$_2$/C electrode not only outperforms a commercial MnO$_2$-based electrode but also approaches Pt/C benchmarks. When integrated into a prototype Al-O$_2$ flow cell, power densities exceeding 250 mW cm^{-2}, CE of ~95%, and SE values above 3.5 kWh kg$_{Al}^{-1}$ can be achieved—surpassing prior Al-air reports. Importantly, DRT analysis has been proven to be a powerful diagnostic tool, uniquely separating anode and cathode charge-transfer processes without the need for a reference electrode. It reveals that anode impedance dominates, highlighting the importance of further anode optimization. In parallel, reducing overall ohmic resistance remains essential for further improving performance. Overall, this study establishes electrode tuning in combination with integrated GDE/full-cell testing as an efficient and broadly applicable strategy for advancing metal-air battery technologies.

CRediT authorship contribution statement

Alexander Rampf: Writing – original draft, Methodology, Investigation, Formal analysis, Data curation, Conceptualization. **Robert Leiter:** Writing – review & editing, Investigation. **Simon Fleischmann:** Writing – review & editing, Investigation. **Giuseppe Antonio Elia:** Writing – review & editing, Funding acquisition. **Roswitha Zeis:** Writing – review & editing, Supervision, Funding acquisition, Conceptualization.

Declaration of competing interest

The authors declare that they have no known competing financial interests or personal relationships that could have appeared to influence the work reported in this paper.

Acknowledgments

Appendix A. Supplementary material

Supplementary material to this article can be found online at https://doi.org/10.1016/j.jechem.2025.10.028.

References

[1] G.A. Elia, K. Marquardt, K. Hoeppner, S. Fantini, R. Lin, E. Knipping, W. Peters, J.F. Drillet, S. Passerini, R. Hahn, Adv. Mater. 28 (2016) 7564–7579.
[2] C. Xu, X. Liu, O. Sumińska-Ebersoldt, S. Passerini, Batter. Supercaps 7 (2024) e202300590.
[3] P. Goel, D. Dobhal, R.C. Sharma, J. Energy Storage 28 (2020) 101287.
[4] M.F. Gaele, T.M. Di Palma, Energy Fuels 36 (2022) 12875–12895.
[5] J. Ryu, M. Park, J. Cho, Adv. Mater. 31 (2019) 1804784.
[6] R. Buckingham, T. Asset, P. Atanassov, J. Power Sources 498 (2021) 229762.
[7] R. Zhao, P. He, F. Yu, J. Yang, Z. Sun, W. Hu, J. Energy Storage 73 (2023) 108985.
[8] A.S. Yasinskiy, S.K. Padamata, P.V. Polyakov, A.V. Shabanov, Non-Ferr. Met. 1 (2020) 15–23.
[9] C. Xu, N. Herrmann, X. Liu, B. Horstmann, S. Passerini, J. Power Sources 574 (2023) 233172.
[10] X. Ge, A. Sumboja, D. Wuu, T. An, B. Li, F.W.T. Goh, T.S.A. Hor, Y. Zong, Z. Liu, ACS Catal. 5 (2015) 4643–4667.
[11] A. Rampf, M. Braig, S. Passerini, R. Zeis, ChemElectroChem 12 (2025) e202400563.
[12] E. Marra, B. Eriksson, T. Novalin, G. Lindbergh, R.W. Lindström, C. Lagergren, J. Electrochem. Soc. 172 (2025) 044514.
[13] R. Yang, Y. Fan, R. Ye, Y. Tang, X. Cao, Z. Yin, Z. Zeng, Adv. Mater. 33 (2021) 2004862.
[14] F. Cheng, Y. Su, J. Liang, Z. Tao, J. Chen, Chem. Mater. 22 (2010) 898–905.
[15] Y. Tang, S. Zheng, Y. Xu, X. Xiao, H. Xue, H. Pang, Energy Storage Mater. 12 (2018) 284–309.
[16] K.A. Stoerzinger, M. Risch, B. Han, Y. Shao-Horn, ACS Catal. 5 (2015) 6021–6031.
[17] D.K. Walanda, G.A. Lawrance, S.W. Donne, J. Power Sources 139 (2005) 325–341.
[18] H. Wang, Z. Lu, D. Qian, Y. Li, W. Zhang, Nanotechnology 18 (2007) 115616.
[19] G.S. Wang, S. He, X. Luo, B. Wen, M.M. Lu, L. Guo, M.S. Cao, RSC Adv. 3 (2013) 18009–18015.
[20] S.K. Meher, G.R. Rao, J. Power Sources 215 (2012) 317–328.
[21] P. Wang, Y.J. Zhao, L.X. Wen, J.F. Chen, Z.G. Lei, Ind. Eng. Chem. Res. 53 (2014) 20116–20123.
[22] Y. Li, J. Wang, Y. Zhang, M.N. Banis, J. Liu, D. Geng, R. Li, X. Sun, J. Colloid Interface Sci. 369 (2012) 123–128.
[23] F. Wang, Y. Zheng, Q. Chen, Z. Yan, D. Lan, E. Lester, T. Wu, Coord. Chem. Rev. 500 (2024) 215537.
[24] M. Rittiruam, P. Buapin, T. Saelee, P. Khajondetchairit, S. Kheawhom, B. Alling, S. Praserthdam, A. Ektarawong, P. Praserthdam, J. Alloys Compd. 926 (2022) 166929.
[25] B. Lan, X. Zheng, G. Cheng, J. Han, W. Li, M. Sun, L. Yu, Electrochim. Acta 283 (2018) 459–466.
[26] N.P. Arias, M.E. Becerra, O. Giraldo, Nanomaterials 9 (2019) 1156.
[27] A.K. Worku, D.W. Ayele, N.G. Habtu, M.D. Ambaw, Heliyon 8 (2022) e10960.
[28] B. Xu, H. Lu, W. Cai, Y. Cao, Y. Deng, W. Yang, Electrochim. Acta 305 (2019) 360–369.
[29] S. Sun, H. Miao, Y. Xue, Q. Wang, S. Li, Z. Liu, Electrochim. Acta 214 (2016) 49–55.
[30] A. Bekisch, K. Skadell, D. Poppitz, M. Schulz, R. Weidl, M. Stelter, J. Electrochem. Soc. 167 (2020) 144502.
[31] A. Bekisch, K. Skadell, J. Ast, M. Schulz, R. Weidl, S. Christiansen, M. Stelter, Int. J. Hydrogen Energy 50 (2024) 1523–1535.
[32] J.A. Vigil, T.N. Lambert, J. Duay, C.J. Delker, T.E. Beechem, B.S. Swartzentruber, ACS Appl. Mater. Interfaces 10 (2018) 2040–2050.
[33] G. Chen, J. Sunarso, Y. Zhu, J. Yu, Y. Zhong, W. Zhou, Z. Shao, ChemElectroChem 3 (2016) 1760–1767.
[34] Z. Khan, S. Park, S.M. Hwang, J. Yang, Y. Lee, H.K. Song, Y. Kim, H. Ko, NPG Asia Mater. 8 (2016) e294.
[35] S. Tang, G. Sun, J. Qi, S. Sun, J. Guo, Q. Xin, G.M. Haarberg, Chin. J. Catal. 31 (2010) 12–17.
[36] S. Möller, S. Barwe, J. Masa, D. Wintrich, S. Seisel, H. Baltruschat, W. Schuhmann, Angew. Chem. Int. Ed. 59 (2020) 1585–1589.
[37] C. Plank, T. Rüther, L. Jahn, M. Schamel, J.P. Schmidt, F. Ciucci, M.A. Danzer, J. Power Sources 594 (2024) 233845.
[38] A. Weiß, S. Schindler, S. Galbiati, M.A. Danzer, R. Zeis, Electrochim. Acta 230 (2017) 391–398.
[39] R. Franke-Lang, J. Kowal, Batteries 7 (2021) 56.

[40] J. Chen, E. Quattrocchi, F. Ciucci, Y. Chen, Chem 9 (2023) 2267–2281.
[41] L. Nagy, H.S. Üneri, M.Á. Kordován, T. Nagy, Á. Kuki, D. Nyul, P. Pál, Z. Erdélyi, M. Zsuga, S. Kéki, J. Electrochem. Soc. 171 (2024) 040509.
[42] T. Wang, X. Pan, J. Chen, Y. Chen, J. Phys. Chem. Lett. 12 (2021) 4799–4804.
[43] A. Subhakumari, T. Thomas, N.P.B. Aetukuri, ACS Energy Lett. 9 (2024) 6109–6116.
[44] J. Chen, H. Zhang, F. Yu, Y. Chen, ACS Appl. Mater. Interfaces 16 (2024) 26226–26233.
[45] D. Ma, J. Chen, F. Yu, Y. Chen, Batter. Supercaps 7 (2024) e202400257.
[46] A. Rampf, C. Marchfelder, R. Zeis, Electrochim. Acta 514 (2025) 145583.
[47] A.R. Mainar, L.C. Colmenares, O. Leonet, F. Alcaide, J.J. Iruin, S. Weinberger, V. Hacker, E. Iruin, I. Urdanpilleta, J.A. Blazquez, Electrochim. Acta 217 (2016) 80–91.
[48] D.K. Walanda, G.A. Lawrance, S.W. Donne, J. Solid State Chem. 182 (2009) 1336–1342.
[49] Y.Z. Shen, Y. Wang, Y.C. Li, Y. Liang, Int. J. Electrochem. Sci. 19 (2024) 100458.
[50] M.A. Danzer, Batteries 5 (2019) 53.
[51] W. Li, X. Cui, R. Zeng, G. Du, Z. Sun, R. Zheng, S.P. Ringer, S.X. Dou, Sci. Rep. 5 (2015) 8987.
[52] W.M. Dose, S.W. Donne, Mater. Sci. Eng. B 176 (2011) 1169–1177.
[53] T. Hatakeyama, N.L. Okamoto, T. Ichitsubo, J. Solid State Chem. 305 (2022) 122683.
[54] T. Soboleva, K. Malek, Z. Xie, T. Navessin, S. Holdcroft, ACS Appl. Mater. Interfaces 3 (2011) 1827–1837.
[55] H.M. Yu, C. Ziegler, M. Oszcipok, M. Zobel, C. Hebling, Electrochim. Acta 51 (2006) 1199–1207.
[56] W. Bin Tu, L.N. Song, S. Liang, Y. Wang, Y. Sun, H.F. Wang, J.J. Xu, Adv. Energy Mater. 15 (2025) 2404946.
[57] K. Shi, Z. Ren, Z. Meng, X. Feng, ChemCatChem 16 (2024) e202301308.
[58] F. Mack, T. Morawietz, R. Hiesgen, D. Kramer, V. Gogel, R. Zeis, Int. J. Hydrogen Energy 41 (2016) 7475–7483.
[59] A. Schiefer, M. Heinzmann, A. Weber, Fuel Cells 20 (2020) 499–506.
[60] S. Gottesfeld, J. Electrochem. Soc. 169 (2022) 124518.
[61] M. Ciureanu, H. Wang, J. Electrochem. Soc. 146 (1999) 4031–4040.
[62] P. Naskar, A. Saha, B. Biswas, A. Banerjee, J. Electrochem. Soc. 171 (2024) 010515.
[63] J. Ryu, H. Jang, J. Park, Y. Yoo, M. Park, J. Cho, Nat. Commun. 9 (2018) 3715.
[64] P. Teabnamang, W. Kao-Ian, M.T. Nguyen, T. Yonezawa, R. Cheacharoen, S. Kheawhom, Energies (Basel) 13 (2020) 2275.
[65] Y. Xue, H. Miao, S. Sun, Q. Wang, S. Li, Z. Liu, RSC Adv. 7 (2017) 5214–5221.
[66] S. Liu, Z. Cao, Y. Meng, Y. Li, W. Yang, Z. Chang, W. Liu, X. Sun, ACS Appl. Mater. Interfaces 13 (2021) 26853–26860.
[67] L. Zhang, D. Fieser, B. Bera, D. Aaron, M.M. Mench, A. Hu, Y. Li, J. Chen, Z. Feng, A. Gulino, G. Compagnini, J. Power Sources 589 (2024) 233752.
[68] H. Wen, Z. Liu, J. Qiao, R. Chen, R. Zhao, J. Wu, G. Qiao, J. Yang, Int. J. Energy Res. 44 (2020) 7568–7579.
[69] J. Gao, Y. Li, Z. Yan, Q. Liu, Y. Gao, C. Chen, B. Ma, Y. Song, E. Wang, J. Power Sources 412 (2019) 63–70.
[70] N. Bevilacqua, M.A. Schmid, R. Zeis, J. Power Sources 471 (2020) 228469.
[71] L. Wang, W. Wang, G. Yang, D. Liu, J. Xuan, H. Wang, M.K.H. Leung, F. Liu, Int. J. Hydrog. Energy 38 (2013) 14801–14809.
[72] M. Heinzmann, A. Weber, E. Ivers-Tiffée, J. Power Sources 402 (2018) 24–33.
[73] S.H. Yang, H. Knickle, J. Power Sources 124 (2003) 572–585.
[74] T.G. Bergmann, N. Schlüter, ChemPhysChem 23 (2022) e202200012.